*J. Fluid Mech.* (2002), *vol.* 461, *pp.* 127–154.  
DOI: 10.1017/S0022112002008273 Printed in the United Kingdom

# Experiments on the motion of gas bubbles in turbulence generated by an active grid

By R. E. G. POORTE† AND A. BIESHEUVEL

J. M. Burgers Centre for Fluid Mechanics, University of Twente,
PO Box 217, 7500 AE Enschede, The Netherlands

(Received 24 October 2000 and in revised form 18 December 2001)

The random motion of nearly spherical bubbles in the turbulent flow behind a grid is studied experimentally. In quiescent water these bubbles rise at high Reynolds number. The turbulence is generated by an active grid of the design of Makita (1991), and can have turbulence Reynolds number $R_\lambda$ of up to 200. Minor changes in the geometry of the grid and in its mode of operation improves the isotropy of the turbulence, compared with that reported by Makita (1991) and Mydlarski & Warhaft (1996). The trajectory of each bubble is measured with high spatial and temporal resolution with a specially developed technique that makes use of a position-sensitive detector. Bubble statistics such as the mean rise velocity and the root-mean-square velocity fluctuations are obtained by ensemble averaging over many identical bubbles. The resulting bubble mean rise velocity is significantly reduced (up to 35%) compared with the quiescent conditions. The vertical bubble velocity fluctuations are found to be non-Gaussian, whereas the horizontal displacements are Gaussian for all times. The diffusivity of bubbles is considerably less than that of fluid particles. These findings are qualitatively consistent with results obtained through theoretical analysis and numerical simulations by Spelt & Biesheuvel (1997).

## 1. Introduction

Fundamental to the understanding of turbulent dispersed two-phase flows is knowledge of the Lagrangian statistics of particles, droplets or gas bubbles and their relationship to the Eulerian statistics of the turbulent flow fields. A classic study on this topic was carried out by Snyder & Lumley (1971). They introduced small solid particles with different sizes and densities (corn, copper, hollow glass, solid glass) in decaying isotropic turbulence behind a grid in a vertical wind tunnel. From the trajectories the particle velocity autocorrelation functions were calculated, for which corrections had to be applied to account for the decay of the turbulent flow field.

The experimental work discussed in our paper resembles that of Snyder & Lumley (1971). It is concerned with the statistics of the motion of gas bubbles in grid-generated turbulence in a vertical water tunnel. The bubbles have diameters of about 1.0 mm, so that in quiescent water they rise rectilinearly with a speed of about 25 cm $s^{-1}$ (hence at a Reynolds number of the order 250) while maintaining an approximately spherical shape. An analysis of this problem, together with results from numerical simulations, has recently been presented by Spelt & Biesheuvel (1997). In part, our study is aimed at providing an experimental check on that theoretical work.

† Present address: Shell International Exploration and Production BV, PO Box 60, 2280 AB Rijswijk, The Netherlands.

Compared with Snyder & Lumley (1971), the present study avoids analysing large numbers of photographs to determine the trajectories and applying corrections for the decay of the turbulence. This is achieved by letting the bubble rise upwards towards the grid through which the water is flowing downwards. By adjusting the mean velocity of the water the bubble can be made to move randomly within in a relatively small interrogation section at an arbitrary position behind the grid. Sampling the position of the bubble with a CCD camera in order to calculate its Lagrangian statistics would require excessively large image processing time and data storage. Hence an alternative method is developed herein based on that employed by Call & Kennedy (1991). They illuminated part of the test section with a laser and projected the light scattered from droplets in an air jet onto a special type of photo multiplier. This method is very efficient because the position of the droplets can be retrieved directly from the analogue signals of the photo multiplier. We have improved its accuracy by employing a specially designed position-sensitive detector, rather than the quadrant detector used by Call & Kennedy (1991).

In order to allow significant intensity of the turbulence (hence a sufficiently large turbulence Reynolds number $R_\lambda$) and variation in the lengthscales of the turbulence an active grid such as designed by H. Makita and his colleagues (Makita 1991; Makita & Sassa 1991) was used. The rods of this bi-plane grid have agitator wings attached to them which are actively flapped in a random manner. As shown by Makita (1991), Makita & Sassa (1991) and Mydlarski & Warhaft (1996), and herein, the structure of the turbulence that is generated conveniently depends on the mode of operation of the grid. Typically, it has much higher intensity and larger lengthscales (exceeding the mesh width) than the turbulence behind a conventional static grid, and so larger values of $R_\lambda$ can be obtained. The isotropy, as measured by the one-point and two-point velocity correlation functions, is not as good as that in the flow behind static grids, but was improved herein by simple methods.

The paper is organized as follows. The main results of the analytical work of Spelt & Biesheuvel (1997) on the motion of bubbles in isotropic turbulence are first summarized in § 2. The experimental facility and diagnostics are described next in § 3. This includes novel aspects of the design and performance of active grids, and a new technique of bubble tracking. In § 4 the experimental results are presented and compared with theoretical predictions. These concern statistical properties such as the mean rise velocity and the variance of the velocity fluctuations of the bubbles. It will be shown that the rise velocity of the bubbles can be significantly reduced, by as much as 35%. The horizontal bubble displacements are found to be Gaussian for all times; the vertical displacements on the other hand show a slight departure from Gaussianity. The bubble diffusion coefficients are significantly smaller than those of fluid particles. There is a reasonable agreement between theory and experiments.

## 2. Theory for spherical bubbles in weak turbulence

The mean rise velocity and diffusivity of spherical bubbles in isotropic turbulence were calculated analytically by Spelt & Biesheuvel (1997, referred to herein as SB) for the special case of turbulence of weak intensity. They are summarized in this section and compared with the experiments in § 4.

For a spherical bubble rising at high Reynolds number in a turbulent liquid flow a reasonably accurate equation of motion is (Sene, Hunt & Thomas 1994; Auton, Hunt & Prud'homme 1998)

$$\frac{\mathrm{d}\boldsymbol{V}}{\mathrm{d}t} = 3\frac{\mathrm{D}\boldsymbol{U}}{\mathrm{D}t} - (\boldsymbol{V}-\boldsymbol{U})\times\boldsymbol{\Omega} - \frac{1}{\tau_b}(\boldsymbol{V}-\boldsymbol{U}) - 2\boldsymbol{g}, \tag{1}$$

where $\boldsymbol{V}(t)$ is the bubble velocity at time $t$, $\boldsymbol{U} = \boldsymbol{U}(\boldsymbol{X}(t), t)$ denotes the liquid velocity and $\mathrm{D}/\mathrm{D}t$ its material derivative at the position $\boldsymbol{X}(t)$ of the bubble, $\boldsymbol{\Omega} = \boldsymbol{\nabla} \times \boldsymbol{U}$ is the vorticity of the liquid at the position of the bubble, $\boldsymbol{g}$ is the acceleration due to gravity and $\tau_b$ ($= a^2/18\nu = V_T/2g$) is a time constant ($a$ is the bubble radius, $\nu$ is the kinematic viscosity of the liquid, and $V_T$ is the terminal rise velocity of a bubble in still fluid). Support for the use of this equation is given by Legendre & Magnaudet (1998).

A lengthscale $\mathscr{L}$ is defined in terms of the Eulerian energy spectrum function of the turbulence $E(k)$ as

$$\frac{1}{\mathscr{L}} \equiv \int_0^\infty kE(k)\mathrm{d}k \Big/ \int_0^\infty E(k)\mathrm{d}k, \tag{2}$$

and a non-dimensional turbulence intensity $\beta$ and a non-dimensional lengthscale $\mathscr{L}^*$ by

$$\beta \equiv \frac{u_0}{V_T}, \quad \mathscr{L}^* \equiv \frac{\mathscr{L}}{\tau_b V_T},$$

in which $u_0$ is the root-mean-square fluid velocity fluctuation The present work is restricted to the special case of weak turbulence of 'intermediate' lengthscales, i.e.

$$\beta \ll 1, \quad \beta \ll \mathscr{L}^* \ll \frac{1}{\beta}, \tag{3}$$

for which it is possible to simplify the equation of motion, and to calculate analytically the mean rise velocity $\overline{V}$ of a bubble using a method proposed by Maxey (1987) for rapidly settling small solid particles. The result is

$$\overline{V} - V_T \simeq -\frac{\pi}{2} \int_0^\infty kE(k)\mathrm{d}k, \tag{4}$$

which can be rewritten using (2) and

$$\tfrac{3}{2}u_0^2 = \int_0^\infty E(k)\mathrm{d}k, \tag{5}$$

as

$$\frac{\overline{V} - V_T}{V_T} \simeq -\tfrac{3}{4}\pi\beta^2 \frac{1}{\mathscr{L}^*}. \tag{6}$$

This explicitly shows the role of $\mathscr{L}^*$ and hence of $\mathscr{L}$. Result (6) expresses that a spherical bubble moving at high Reynolds number is on average slowed down by isotropic turbulence. As explained by SB, bubbles move under the action of fluctuating lift forces in a lateral direction towards regions where the downward fluid velocity has a maximum and the upward fluid velocity has a minimum. This slows down the bubbles because (i) viscous forces make the bubbles adapt their speed to the fluid velocity fluctuations, which on average are directed downwards along the bubble path, and (ii) the lateral motion induces a lift force in the downward direction.

The magnitude of $\mathscr{L}^*$ depends on the spectrum. SB performed numerical experiments in isotropic turbulence with a Kraichnan spectrum function and a von Kármán–Pao spectrum function, generated by the method of Kinematic Simulation (Fung *et al.* 1992), for values up to $\beta = 1$. They found excellent agreement with (6) for small values of $\beta$. Some experimental support for the slowing down of high-Reynolds-number bubbles exists (Eppinger 1995), but (6) has not yet been checked explicitly.

The dispersion of the bubbles can be quantified by a diffusivity. SB calculated this statistic under the same assumptions as above and found that the vertical diffusivity is given by

$$\mathscr{D}_x(\infty) \simeq \beta u_0 L_{11}, \tag{7}$$

with $L_{11}$ the longitudinal integral scale of the turbulence, and the horizontal diffusivity by

$$\mathscr{D}_y(\infty) \simeq \tfrac{1}{2}\beta u_0 L_{11} + \tfrac{1}{4}\pi\tau_b^2 V_T \int_0^\infty kE(k)\mathrm{d}k. \tag{8}$$

Introducing the non-dimensional integral scale $\mu = L_{11}/(\tau_b V_T)$, the latter expression can also be written as

$$\mathscr{D}_y(\infty) \simeq \tfrac{1}{2}\beta u_0 L_{11}\left(1 + \frac{3\pi}{4\mu\mathscr{L}^*}\right). \tag{9}$$

These results coincide with the corresponding expressions for small solid particles (Csanady 1963; Nir & Pismen 1979) except for the second term on the right-hand sides of (8) and (9), a term that increases the lateral diffusivity and which is associated with the lift forces acting on the bubbles. In weak turbulence with large characteristic lengthscales the contribution due to the lift forces on high-Reynolds-number bubbles is not important, and in that case the diffusivities of the gas bubbles are identical to those of small solid particles, with the lateral diffusivity being half the longitudinal diffusivity.

A discussion of the dispersion of high-Reynolds-number bubbles in isotropic turbulence of high intensity ($\beta \simeq 1$) and large characteristic lengthscales ($\mathscr{L}^* \gg 1$) may be found in Spelt & Biesheuvel (1998). The case of low-Reynolds-number bubbles in isotropic turbulence of very high intensity ($\beta \gg 1$), when lift forces are also not important but the acceleration reaction of the bubbles plays a significant role, was studied by Wang & Maxey (1993*a*) and Maxey, Chang & Wang (1994). The literature on the gravitational settling and dispersion of small solid particles in turbulent flows is extensive; examples of studies that are relevant to the present work include Mei, Adrian & Hanratty (1991, 1997), Wang & Maxey (1993*b*) and Mei (1994).

## 3. Experimental facility and diagnostics

The experimental facility and the measurement techniques are described in this section. The water tunnel, the apparatus that generates the gas bubbles, the methods to determine the parameters that characterize the gas bubbles and the turbulence are discussed briefly; the configuration and performance of the active grid and the bubble tracking device, comparitively novel techniques, are described in more detail. A more extensive discussion is given in the thesis of Poorte (1998), on which this paper is based.

### 3.1. *Water tunnel*

A recirculating water tunnel with a vertical test section was used in the experiments. The length of the test section is 2.00 m, its width is $0.45 \times 0.45\,\mathrm{m}^2$. Three walls are made of 19 mm thick glass. The fourth wall is made of stainless steel, and through three portholes in this wall probes can be installed in the test section.

The instantaneous volume flow rate was measured with an electromagnetic flowmeter (Danfoss Magflo Mag 3100). A computer controlled pump (Egger RPP 300)

delivered a time-average volume flow rate of 0.049–0.49 m s$^{-1}$ in the test section, constant within 0.6%.

Free-stream turbulence, swirl and non-uniformities in the mean flow are reduced by suitably chosen screens and a smooth contraction of area ratio 4. Without the turbulence generator, the mean velocity was uniform within $\pm 2.0\%$, while the turbulence intensity was less than 1.2% in the core region (82% of the width of the test section).

The tunnel was filled with tap water, that was de-ionized first to remove calcium-ions that would turn the windows of the test section opaque. The water was refreshed about every 4 weeks. To remove contamination as much as possible, the water was filtered continuously through a bypass at a rate of about 10 l min$^{-1}$. Bubbles that are injected in the test section will ultimately be transported to other parts of the water tunnel. These bubbles were removed by a passive bubble trap.

### 3.2. *Measurement of the turbulence velocity field*

The turbulence velocity field (without the bubbles) was measured with a two-component backscatter LDV system (Dantec) using the particles that were naturally present in the water as seeding. It was verified that a correction for velocity bias was not necessary.

Moments of the velocity components, up to fourth-order, were calculated using modified versions of software developed at the Technical University of Delft. Two-point correlations were calculated with the slotting technique with local normalization (Tummers & Passchier 1996), assuming the validity of Taylor's frozen turbulence hypothesis (the largest turbulence intensity is 19.3%). Direct estimates of energy spectra were determined by an FFT with variable windowing of the measured correlation function, while the method proposed by van Maanen & Oldenziel (1998) was used to estimate the high-frequency parts. Here one first fits an analytic function with six free parameters to the measured autocorrelation function and subsequently transforms that fit analytically. Compared to a direct calculation, this method increases the accuracy of the spectral estimate considerably for high frequencies.

The longitudinal integral scale was computed from the measured autocorrelation coefficient:

$$L_{11} = U \int_0^\infty \frac{\overline{u(t)u(t+\tau)}}{(\overline{u(t)^2 u(t+\tau)^2})^{1/2}} \mathrm{d}\tau,$$

where $U$ is the mean streamwise velocity and $u$ is the streamwise velocity fluctuation; in what follows $v$ denotes the lateral velocity fluctuation. The dissipation of turbulent kinetic energy $\epsilon$ was computed both from the transport equation for the turbulent kinetic energy (in which it is permissible to neglect the terms related to velocity skewness and pressure–velocity correlations)

$$U \frac{\mathrm{d}}{\mathrm{d}x}\left(\frac{3}{2}u_0^2\right) = -\epsilon,$$

with $u_0^2 = (\overline{u^2 + 2v^2})/3$, assuming lateral homogeneity, and from

$$\epsilon = 15\nu \int_0^\infty k_1^2 F_{11}(k_1)\, \mathrm{d}k_1,$$

where $k_1$ is the longitudinal wavenumber and $F_{11}(k_1)$ is the streamwise power spectrum of the longitudinal velocity fluctuations $u$. The two estimates of $\epsilon$ were within 5%.

The Taylor microscale $\lambda$ was determined from

$$\epsilon = 15\nu \frac{u_0^2}{\lambda^2},$$

valid for isotropic turbulence, and the Kolmogorov lengthscale, timescale and velocity scale were estimated from their definitions

$$\eta_K = \left(\frac{\nu^3}{\epsilon}\right)^{1/4}, \quad \tau_K = \left(\frac{\nu}{\epsilon}\right)^{1/2}, \quad v_K = (\nu\epsilon)^{1/4}.$$

Finally, the lengthscale $\mathscr{L}$ was computed from

$$\frac{1}{\mathscr{L}} = -\frac{16}{3\pi}\int_0^\infty \frac{1}{r}\frac{\partial f}{\partial r}\,\mathrm{d}r,$$

in which $f(r)$ is the longitudinal velocity correlation. This expression can be shown (Spelt 1996) to be equivalent to the definition (2) and is more convenient to evaluate, as an analytical expression for $f$ and its derivative is available from the van Maanen & Oldenziel (1998) algorithm mentioned above.

The experimental uncertainties in $\mathscr{L}$, $\mu$ and $\lambda$ were 6%, 5% and 3% respectively; those in $U$ and $u_0$ were 1.6% and 3% (95% confidence level).

### 3.3. *Active grid*

#### 3.3.1. *Grid specifications and forcing protocols*

Figure 1 shows photographs of our active grid. Its design follows that of the grids of Makita (Makita 1991; Makita & Sassa 1991) and Mydlarski & Warhaft (1996), though there are some variations. Table 1 gives the grid specifications. The bars of these bi-plane grids have agitator wings, and by rotating each of the grid bars in a controlled way (the forcing protocol) a flapping motion of the wings with specified statistics can be created. In the *synchronous mode* of operation the rods have constant angular velocity $\Omega_m$, equal in magnitude but with opposite sign (i.e. direction of rotation) for adjacent rods. In the studies mentioned above another forcing protocol was also used in which the rods have angular velocities $\Omega_m$ or $-\Omega_m$ for a duration of time that is chosen randomly, say from a set $[\Delta T_{min}, \Delta T_{max}]$; we will refer to this as the *single-random asynchronous mode* of operation. For reasons explained below, we have also tried a new forcing protocol in which both the rotation speed and the duration are chosen randomly from the sets $[-\Omega_m, \Omega_m]$ and $[\Delta T_{min}, \Delta T_{max}]$, respectively; this the *double-random asynchronous mode* of operation.

The grid-generated turbulence in the earlier studies appeared to have some deficiencies which, as will be shown here, can be overcome by simple modifications of the grid geometry and the forcing protocol.

First, Makita (1991) and Mydlarski & Warhaft (1996) report that the turbulence generated by their active grids contains distinct periodicities which appear as spikes in the energy spectrum. This can be understood by considering an active grid working in the synchronous mode with angular velocity $\Omega_m$. The geometry of the grid is invariant under rotation through an angle of $\pi$ rad, so that the fluid streaming through the grid is periodically forced with period $1/(2\Omega_m)$. If the mean velocity of the fluid is $U$, structures with an extent $U/(2\Omega_m)$ in the longitudinal direction will be created at the grid. These structure will fade only partially as the flow develops. Obviously, the energy spectrum would show distinct spikes at frequency $2\Omega_m$, and possibly at higher harmonics.

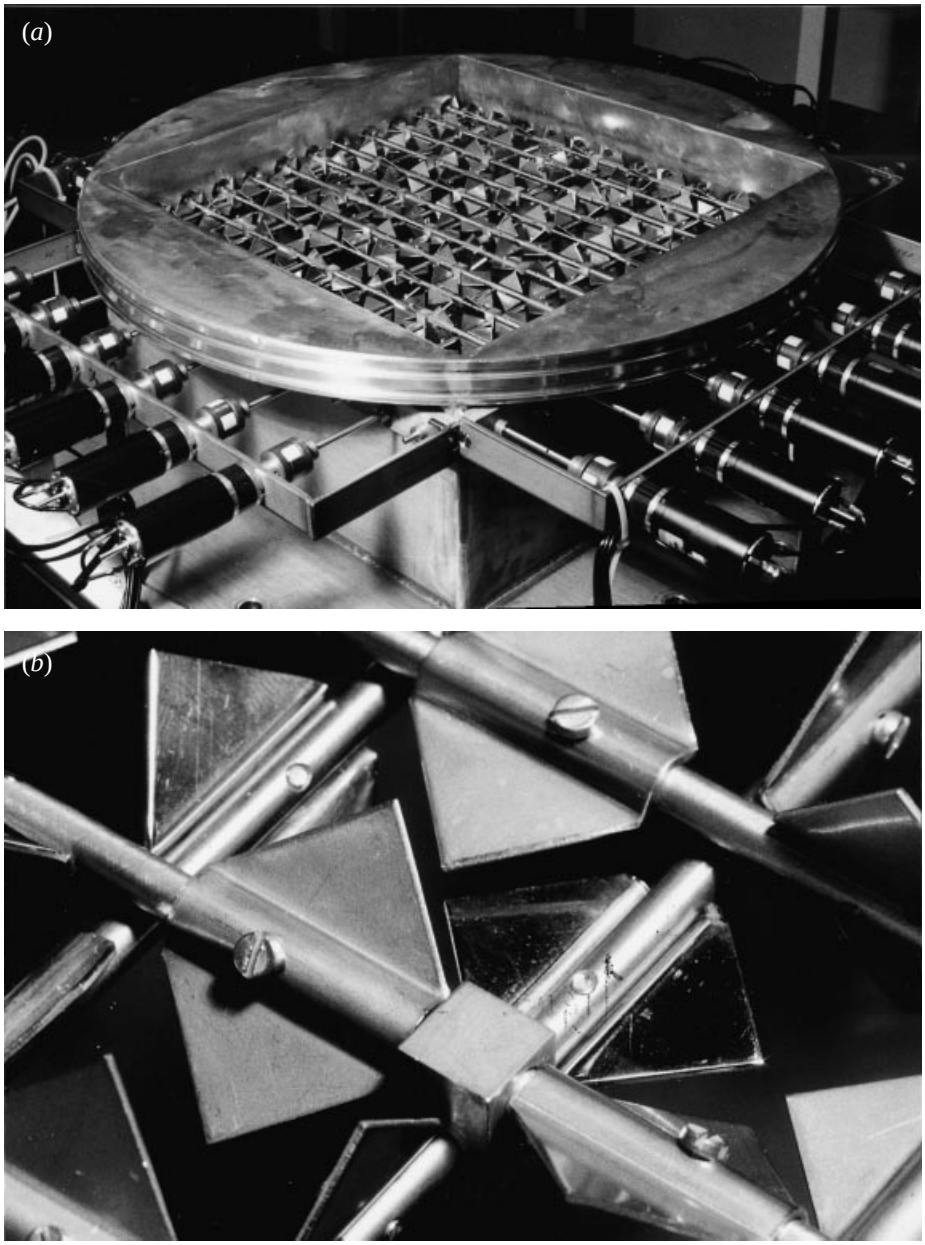


FIGURE 1. The active grid. (*a*) Overview, showing some of the DC motors. (*b*) Details of rods and agitator wings; the wings are mounted in staggered orientation.

Mydlarski & Warhaft (1996) report that the periodicities remain with the single-random asynchronous mode of operation. Note that the probability distribution function of the rotation speed $\Omega$ of such a protocol is

$$\mathrm{pdf}_{SR}(\Omega) = \tfrac{1}{2}\delta(\Omega - \Omega_m) + \tfrac{1}{2}\delta(\Omega + \Omega_m),$$

and so has two spikes, i.e. at $-\Omega_m$ and $\Omega_m$. This means that the flow is still forced predominantly with a single frequency. By contrast, the double-random asynchronous

| | Makita (1991) | Mydlarski & Warhaft (1996) | Present work |
|---|---|---|---|
| Fluid | air | air | water |
| Number of rods | 30 | 16 | 24 |
| Rod diameter (mm) | 6.0 | 6.4 | 5.0 |
| Mesh width $M$ (mm) | 46.7 | 50.8 | 37.5 |
| Wing chord (mm) | 45.3 | 49.0 | 35.4 |
| Wing aspect ratio | 4.0 | 4.0 | 4.0 |
| Wing thickness (mm) | – | 0.38 | 1.0 |
| Mechanical forcing | stepping motors | stepping motors | DC motors |
| Angular velocity $\Omega$ (r.p.s.) | 2.0 | 2.0–4.0 | 0.2–12.8 |
| Test section width | $15M \times 15M$ | $8M \times 8M$ | $12M \times 12M$ |
| Test section length | $128M$ | $80M$ | $53M$ |
| Mean velocity $U$ (m s$^{-1}$) | 5.0 | 3.2–14.3 | 0.30 |
| $Re_M = UM/\nu$ | $15.6 \times 10^3$ | $10–48 \times 10^3$ | $11.3 \times 10^3$ |

TABLE 1. Main characteristics of active grids.

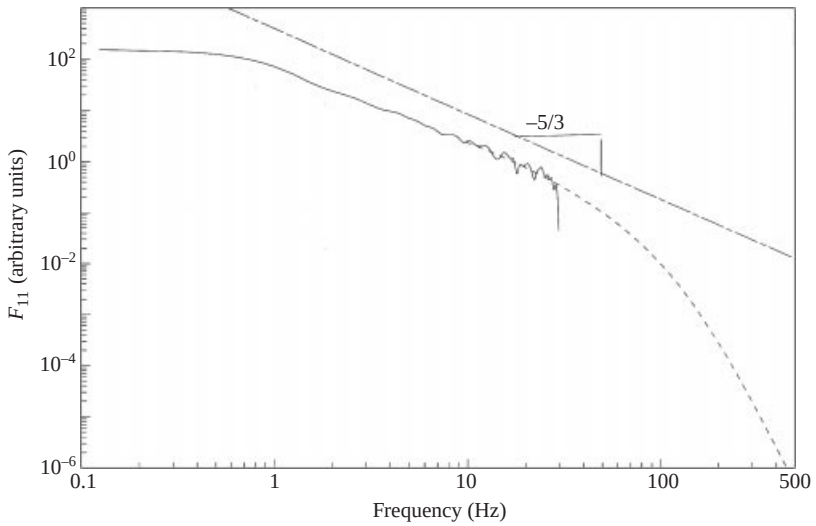


FIGURE 2. Longitudinal one-dimensional energy spectrum measured at $x/M = 11.8$ and grid Reynolds number $Re_M = 11\,250$ with the double-random asynchronous mode of operation DR2 ($\Omega_m = 8.20$ r.p.s., $\Delta T_{min} = 0.05$ s, $\Delta T_{max} = 0.24$ s). The solid curve is the directly computed spectrum, the dotted line is the estimate for high frequencies obtained with the van Maanen & Oldenziel (1998) algorithm. The dash dotted line has slope $-5/3$. The vertical axis is in arbitrary units.

mode of operation has a uniform probability distribution function

$$\mathrm{pdf}_{DR}(\Omega) = \begin{cases} 1/(2\Omega_m), & \Omega \in [-\Omega_m, \Omega_m], \\ 0, & \text{elsewhere.} \end{cases}$$

Using this type of forcing protocol it was found that the spectrum was free from periodicities, even close to the grid. A typical example is given in figure 2, which shows the spectrum of case C in table 2.

The second deficiency described in Makita (1991), Makita & Sassa (1991) and

| Case | A | B | C | D | E | F |
|---|---|---|---|---|---|---|
| Protocol | DR1 | DR2 | DR2 | DR3 | DR1 | DR1 |
| $\Omega_m$ (r.p.s.) | 1.37 | 8.20 | 8.20 | 8.20 | 1.37 | 1.37 |
| $\Delta T_{min}$ (s) | 0.05 | 0.05 | 0.05 | 0.05 | 0.05 | 0.05 |
| $\Delta T_{max}$ (s) | 1.46 | 0.24 | 0.24 | 0.73 | 1.46 | 1.46 |
| $Q$ ($\mathrm{l\,s^{-1}}$) | 60.75 | 60.75 | 60.75 | 60.75 | 60.75 | 60.75 |
| $x/M$ | 16.9 | 6.9 | 11.8 | 29.0 | 48.2 | 6.9 |
| $u_0$ ($\mathrm{mm\,s^{-1}}$) | 30.4 | 55.8 | 40.9 | 31.7 | 16.3 | 57.8 |
| $U$ ($\mathrm{mm\,s^{-1}}$) | 306.4 | 296.6 | 299.2 | 303.4 | 316.3 | 294.2 |
| $u_0/U$ % | 9.92 | 18.8 | 13.7 | 10.4 | 5.14 | 19.3 |
| $u'/v'$ | 1.10 | 1.06 | 1.09 | 1.16 | 1.08 | 1.04 |
| $L_{11}$ (mm) | 45.4 | 33.8 | 53.1 | 89.2 | 76.9 | 26.3 |
| $\mathscr{L}$ (mm) | 3.8 | 2.6 | 4.3 | 8.5 | 9.0 | 1.4 |
| $\lambda$ (mm) | 3.9 | 2.8 | 3.7 | 6.4 | 6.5 | 2.5 |
| $\eta_K$ (mm) | 0.18 | 0.11 | 0.15 | 0.24 | 0.32 | 0.10 |
| $\tau_K$ (ms) | 31 | 13 | 23 | 54 | 109 | 11 |
| $v_K$ ($\mathrm{mm\,s^{-1}}$) | 5.7 | 8.6 | 6.6 | 4.3 | 3.0 | 9.7 |
| $R_\lambda$ | 125 | 160 | 158 | 198 | 101 | 143 |
| $S_u$ | 0.14 | 0.22 | 0.16 | 0.14 | 0.08 | 0.23 |
| $F_u$ | 3.03 | 2.92 | 2.99 | 2.79 | 2.88 | 2.90 |

TABLE 2. Experimental conditions: parameters of the grid-generated turbulence. The first three symbols refer to the asynchronous mode of operation of the grid in which the rotation speed of the rods and the duration of that rotation were chosen randomly from the intervals $[-\Omega_m, \Omega_m]$ and $[\Delta T_{min}, \Delta T_{max}]$, respectively. The other symbols indicate the volume flow rate $Q$ in the test section, the distance downstream from the active grid $x/M$, the turbulence intensity $u_0$ and the mean fluid velocity $U$; $L_{11}$ is the longitudinal turbulence integral scale, $\mathscr{L}$ is the intermediate lengthscale defined in (2), $\lambda$ is the Taylor microscale, and $\eta_K$, $\tau_K$ and $v_K$ are the Kolmogorov lengthscale, timescale and velocity scale, respectively. The microscale Reynolds number $R_\lambda$ varies between 101 and 198. The ratio of the r.m.s fluid velocities in the longitudinal and lateral directions $u'/v'$ and the value of the skewness of the streamwise velocity fluctuation, $S_u$, quantify the departure from isotropy. $F_u$ is the flatness of the streamwise velocity fluctuation.

Mydlarski & Warhaft (1996) is the strong anisotropy of the turbulence close behind the active grid. To find the reason for this we carried out a series of experiments with single-random asynchronous modes of operation chosen similar to the ones used in those studies, but with the agitator wings mounted on the rods in a staggered, instead of parallel, arrangement. A parallel orientation of the wings on the grid creates obstructions to the flow that are much larger in the lateral direction ($\simeq 2.5M$) than in the streamwise direction ($\simeq M$). This effect is expected to be less pronounced with a staggered orientation of the wings. This simple change of the grid configuration has a positive effect on the isotropy of the generated turbulence as illustrated in figure 3(*a*), in which data for the downstream evolution of $u'/v' = (\overline{u^2}/\overline{v^2})^{1/2}$, the ratio of the root-mean-square values of the longitudinal and lateral velocity fluctuations, are compared with the data obtained by Makita & Sassa (1991); here both grids worked in the single-random asynchronous mode. Our protocols had identical time structure ($\Delta T_{min} = 0.05\,\mathrm{s}$, $\Delta T_{max} = 0.20\,\mathrm{s}$) while the velocity varied: $\Omega_m = 0.50$, 6.25 and 12.50 r.p.s. for SR1, SR2 and SR3 respectively. A double-random asynchronous mode of operation yields even better results as illustrated in figure 3(*b*), while figure 3(*c*) makes clear that the disadvantage of the staggered wing orientation is a reduction of the turbulence intensity; a consequence of the lower time-average solidity of this configuration. The intensity, though, is still higher than that found with a conventional static grid.

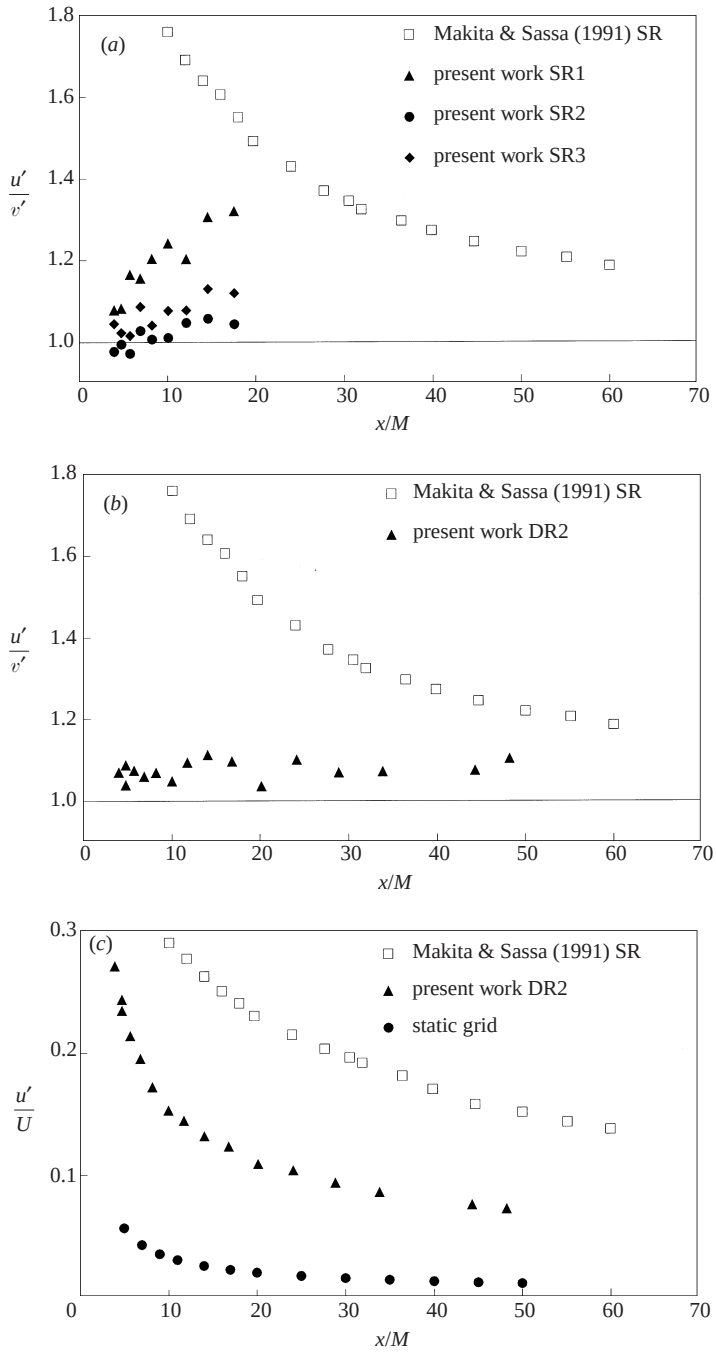


FIGURE 3. Comparison between the performance of the active grid of Makita & Sassa (1991), with parallel orientation of the agigator wings and single-random asynchronous mode of operation, and that of our grid, with staggered wing orientation and the option of a double-random asynchronous mode of operation. (*a*) Downstream evolution of the ratio of the root-mean-square longitudinal and lateral velocity fluctuations in the single-random (SR) mode of operation. $\Omega_m = 0.50$, 6.25 and 12.50 r.p.s. for SR1, SR2 and SR3 respectively. (*b*) As (*a*), but with our grid working in the double-random mode DR2 (table 2). (*c*) Downstream evolution of the root-mean-square streamwise velocity fluctuation.

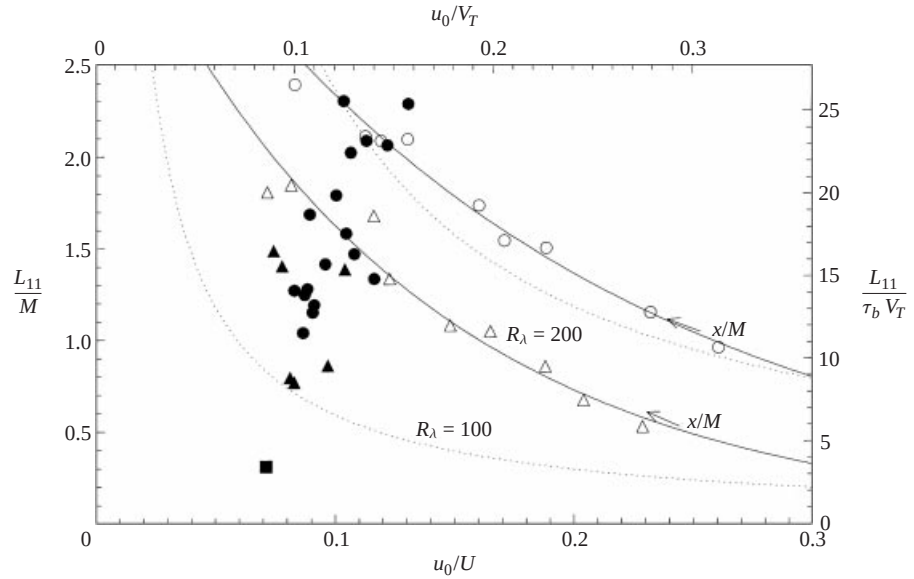


FIGURE 4. Dependence of the macrostructure of the turbulence behind the active grid on the forcing protocol. This structure is represented by the values of the turbulence intensity $u_0$ and the longitudinal integral scale $L_{11}$, made dimensionless by the mesh width $M = 37.5$ mm and the mean fluid velocity $U = 0.30\,\mathrm{m\,s^{-1}}$, or by two parameters associated with a bubble of radius 1.0 mm; the terminal rise velocity $V_T = 0.27\,\mathrm{m\,s^{-1}}$ and the relaxation length $\tau_b V_T = 3.37$ mm. Solid symbols are at fixed downstream position $x/M = 20$ for various modes of operation of the grid (solid triangle: synchronous mode, solid circle: double-random asynchronous mode; solid square: static agitator wings at $\pm 45°$ with mean flow). Open symbols and solid lines are for a fixed forcing protocol but varying downstream position $x/M$ (open triangle: DR2; open circle: DR3). Dotted lines indicate curves of constant turbulence Reynolds number $R_\lambda$. In all cases the grid Reynolds number is $Re_M = 11\,250$.

### 3.3.2. *Grid performance*

By choosing the forcing protocol of the active grid (i.e. the mode of operation, the angular velocity $\Omega_m$ and the time intervals $\Delta T_{min}$ and $\Delta T_{max}$) it is possible to vary the longitudinal integral scale $L_{11}$ and, to a lesser degree, the turbulence intensity $u_0$. This is illustrated in figure 4. For a given protocol (open symbols) the turbulence intensity decreases with distance downstream, while the longitudinal integral scale increases. For every forcing protocol such a decay curve exists (two are shown). Thus, by choosing the forcing protocol and the downstream position $x/M$ it is possible to generate a turbulent velocity field with the desired values of $u_0$ and $L_{11}$, without the need to vary the mean velocity $U$. This makes the active grid a very convenient tool for investigations of the motion of bubbles in grid-generated turbulence, because the velocity and time scales of the turbulence can be changed independently of those of the bubbles. As an example, the values of $\beta = u_0/V_T$ and $\mu = L_{11}/(\tau_b V_T)$ that can be obtained for a bubble with 1 mm diameter are indicated on the axes in figure 4.

The lowest integral scale is obtained if the grid is stationary with the agitator wings at $\pm 45°$ angle of attack with the mean flow. Any motion of the grid, in the regime investigated, leads to a turbulent flow with larger integral scale; the largest scale we could obtain at $x/M = 20$ is about $2.4M$. Since the turbulence intensity $u_0$ and the integral scale $L_{11}$ depend on the forcing protocol so does the turbulence Reynolds number $R_\lambda$, since this varies approximately as $(u_0 L_{11}/\nu)^{1/2}$. We obtained values of $R_\lambda$ between 90 and 200. In figure 4 dotted lines indicate curves of constant $R_\lambda$.

All the experiments on bubble motion in grid-generated turbulence reported below have been performed with the grid working in the double-random asynchronous mode. Three forcing protocols were used, denoted DR1, DR2 and DR3. Values of the angular velocity $\Omega_m$ and the time intervals $\Delta T_{min}$ and $\Delta T_{max}$ of these protocols, together with some of the properties of the turbulence at the various measuring stations $x/M$ are listed in table 2. In all these experiments the grid Reynolds number was $Re_M = 11\,250$.

Figure 5 shows that the turbulence generated by protocol DR1 has good lateral homogeneity, even close to the grid ($x/M = 5$). Similar velocity profiles were obtained for the other protocols at $x/M = 5$ and $x/M = 20$. It was found that in the core region (i.e. $|y/M|, |z/M| \leqslant 4$) of the measuring section: (i) the variations in the mean velocity in the longitudinal direction, $U$, were within 2.0% of the mean centreline velocity, (ii) the variations in the mean velocity in the lateral direction, $V$, were within 1.6% of the mean streamwise centreline velocity, and (iii) the variations of the root-mean-square turbulence velocities in the longitudinal and the lateral directions, $u'$ and $v'$ respectively, were within 5.4% of their value at the centreline. This good homogeneity is attributed to the active mixing of the flow by the agitator wings and the large turbulence diffusivity downstream of the grid.

The decay of the turbulence energy could be described well by a power law of the form

$$\frac{U^2}{u_0^2} = B\left(\frac{x}{M}\right)^n.$$

The values of the decay coefficient $B$ and the decay exponent $n$ was found to be different for each of the protocols: $B = 1.59$, $n = 1.41$ (DR1); $B = 3.51$, $n = 1.04$ (DR2); $B = 4.08$, $n = 0.87$ (DR3). A dependence of the decay coefficient $n$ on the forcing protocol was also noted by Ling & Wan (1972) in their experiments with another type of 'mechanically agitated' grid.

As a further test of the isotropy of the turbulence we measured the longitudinal and lateral velocity correlation functions $f(r)$ and $g(r)$, which for incompressible isotropic turbulence should be related by (e.g. Batchelor 1953)

$$g(r) = f(r) + \tfrac{1}{2} r \frac{\partial f}{\partial r}. \tag{10}$$

The results are shown in figure 6; the solid circles are measured values of $f(r)$, the solid triangles are data for $g(r)$. To check (10) an analytic description of $f(r)$ was first obtained from the data with the van Maanen & Oldenziel (1998) algorithm, then the right-hand side of (10) was evaluated using this description; the result is shown as a solid line. For small separation distances the agreement between the 'isotropic' $g(r)$ calculated in this way and the measured one is good, which suggest that the turbulence is locally isotropic. For larger separations the measured $g(r)$ is slightly lower than the isotropic value, which suggests a small departure from isotropy at the large scales. Nevertheless, the agreement found here is considerably better than that reported previously by Makita (1991).

It appears then that with these modifications the one-point and two-point velocity correlations of the turbulence behind our active grid are close to the isotropic values. This is not true however, for three-point velocity correlations. In isotropic turbulence the skewness of the streamwise velocity component $S(u)$ should be 0 because of invariance under reflection of the coordinate system. For static grids $S(u)$ is typically less than 0.04 at $x/M > 50$ (e.g. Mohamed & LaRue 1990). Turbulence behind active

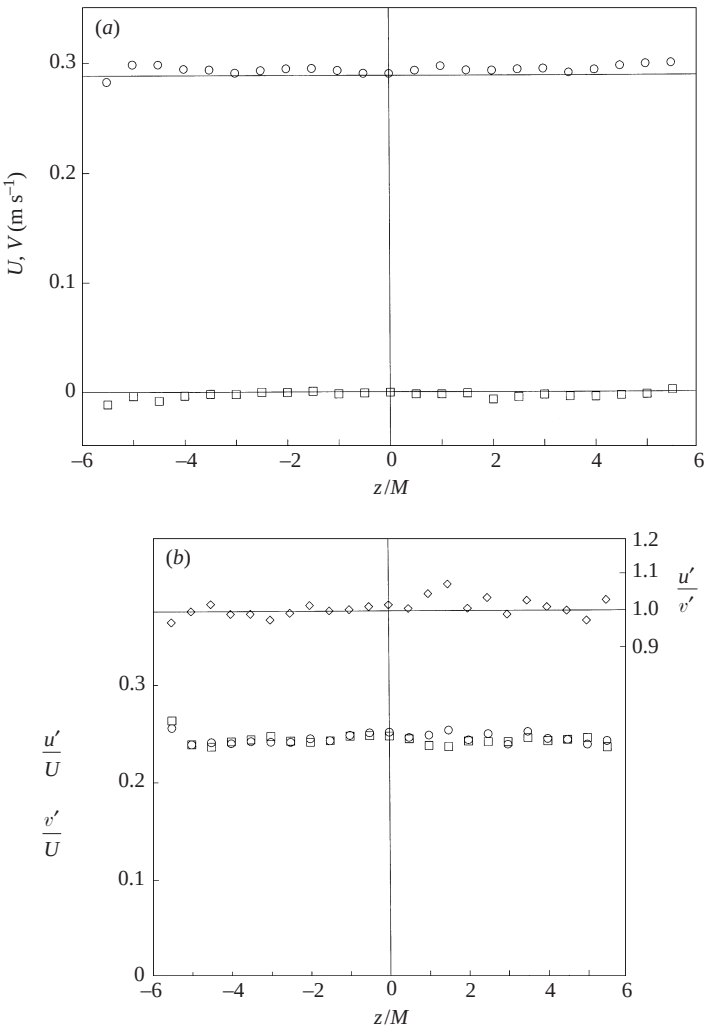


FIGURE 5. Lateral homogeneity of the turbulence at $x/M = 5$, generated with protocol DR1. (*a*) Mean velocities in the streamwise direction ($U$, circle) and the transverse direction ($V$, square). (*b*) Root-mean-square velocity fluctuations in the streamwise direction ($u'/U$, circle) and the transverse direction ($v'/U$, square), and their ratio ($u'/v'$, diamond).

grids displays much larger velocity skewness: Makita (1991) finds a value of 0.188 for $S(u)$ at $x/M = 50$, Mydlarski & Warhaft (1996) report similar values behind their active grid, and we too find $S(u)$ in the range 0.05–0.35, depending on $x/M$ and the type of protocol.

### 3.4. *Bubble generation*

Small bubbles of well-controlled size are generated with the method of Ooi & Acosta (1984). In a separate vessel air is made to flow through a small needle (Hamilton, i.d. 0.15 mm) at a rate that can be finely adjusted between 0.1 and 300 $\text{mm}^3\,\text{s}^{-1}$ with a micrometering valve. This needle is placed vertically in a steady uniform upward liquid flow of low turbulence intensity. By varying the liquid velocity a stream of small bubbles of nearly identical size is generated. The (adjustable) equivalent diameters

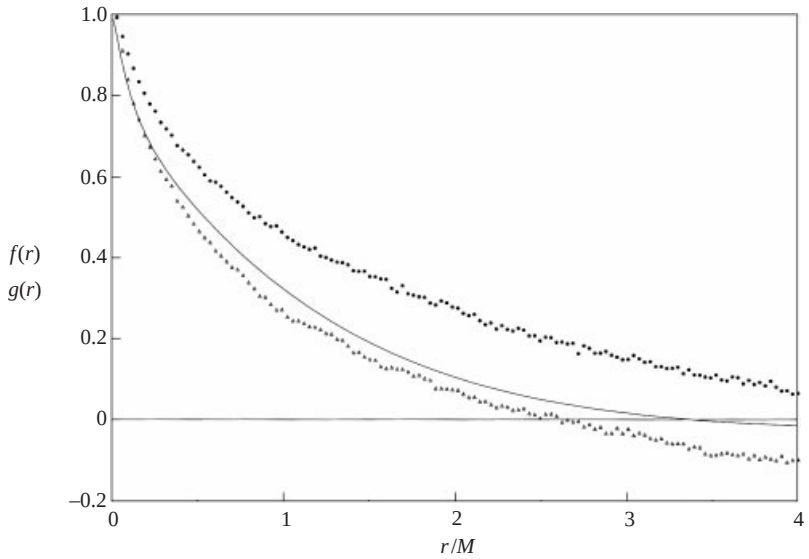


FIGURE 6. Measurements of the longitudinal and lateral velocity correlation functions $f(r)$ (solid circles) and $g(r)$ (triangles). The curve is an estimate of $g(r)$ calculated by applying the relation $g(r) = f(r) + (r/2)\partial f/\partial r$ to an analytic expression for $f(r)$ based on the data. (Protocol DR2 with $x/M = 14.1$, $u_0/U = 12\%$, $R_\lambda = 157$, $Re_M = 11\,250$.)

are between about 0.3 and 1.9 mm. After its generation a bubble rises upwards and is then captured in a funnel, after which it is transported by a small liquid flow (typically less than $100\,\mathrm{cm^3\,s^{-1}}$) through a tube (i.d. 3 mm) into a probe with the same inner diameter. From the probe the bubble is finally injected into the test section at any desired location.

The average size of the bubbles was determined by collecting bubbles, letting typically 20 of them coalesce to form a larger bubble, and then passing that bubble as a plug of gas through a narrow capillary of known inner diameter. The equivalent diameter $a_e$ of the bubbles in the test section can then be inferred from a measurement of the length of the gas plug. The terminal rise velocity of the bubbles in quiescent liquid $V_T$ was measured with the bubble tracking system described below, by averaging over typically 200 bubbles. This was done before and after each experimental run (such a run lasted typically 5 hours). In such an experiment the root-mean-square variation of the rise velocity of the bubbles was always less than 3%; hence, in each experimental run the bubble radius was constant to within $\pm 1.5\%$.

The terminal rise velocities measured (table 3) were 1–15% lower than those found by Duineveld (1995) for bubbles in highly purified water. However, for 'dirty' water the rise velocity of a bubble of 0.57 mm (0.34 mm) would be $0.129\,\mathrm{m\,s^{-1}}$ ($0.076\,\mathrm{m\,s^{-1}}$), according to the findings of Bel Fdhila & Duineveld (1996), which is clearly much lower than the values we obtained. It can thus be concluded that the water in the tunnel is effectively clean. In his thesis Duineveld (1994, p. 127) mentions that bubbles with an equivalent radius larger than about 0.34 mm behave in fresh tap water in the same way as in hyperclean water. It appears then that our water filtering system maintains the water quality at a level of purity which is only slightly less than that of fresh tap water.

The bubbles slowly dissolve into the water, and this was found to noticeably affect the average rise velocity in the turbulent flow some 40 s after injection in the test

| Case | A1 | B1 | C1 | D1 | E1 | F1 | B2 | F2 |
|---|---|---|---|---|---|---|---|---|
| $a_e$ (mm) | 0.57 | 0.57 | 0.57 | 0.57 | 0.57 | 0.57 | 0.34 | 0.34 |
| $V_T$ (m s$^{-1}$) | 0.248 | 0.279 | 0.254 | 0.277 | 0.246 | 0.273 | 0.126 | 0.135 |
| $\tau_b$ (ms) | 15.3 | 17.3 | 15.7 | 17.1 | 15.2 | 16.9 | 6.2 | 6.2 |
| $Re$ | 283 | 318 | 289 | 315 | 280 | 311 | 84 | 91 |
| $We$ | 0.96 | 1.22 | 1.00 | 1.19 | 0.94 | 1.16 | 0.15 | 0.17 |
| $\beta$ | 0.123 | 0.200 | 0.161 | 0.115 | 0.066 | 0.212 | 0.443 | 0.428 |
| $\mu$ | 11.9 | 7.0 | 13.3 | 18.8 | 20.6 | 5.7 | 43.0 | 31.2 |
| $\mathscr{L}^*$ | 0.97 | 0.52 | 1.05 | 1.75 | 2.35 | 0.30 | 2.44 | 1.15 |
| $\lambda^*$ | 1.03 | 0.58 | 0.93 | 1.35 | 1.74 | 0.54 | 3.56 | 2.97 |
| $T$ (s) | 338 | 236 | 625 | 630 | 536 | 475 | 1269 | 462 |
| $N_{valid}$ | 1226 | 1330 | 2830 | 1492 | 1632 | 2403 | 6670 | 2673 |

TABLE 3. Experimental conditions: parameters of the bubbles. The letters A to F refer to the corresponding cases in table 2. The symbols $a_e$, $V_T$ and $\tau_b$ denote, respectively, the equivalent radius, the rise velocity in still fluid and the relaxation time of the bubble, and $Re$ and $We$ are the associated Reynolds number and Weber number. The bubble parameters are related to those of the turbulence through the non-dimensional turbulence intensity $\beta = u_0/V_T$, turbulence integral scale $\mu = L_{11}/(\tau_b V_T)$, intermediate scale $\mathscr{L}^* = \mathscr{L}/(\tau_b V_T)$, and Taylor lengthscale $\lambda^* = \lambda/(\tau_b V_T)$. The total bubble observation time is denoted $T$, and $N_{valid}$ is the number of bubbles in the ensemble used to determine the statistics of the bubble motion.

section. Since the time that elapsed from the injection of a bubble to the end of the measurement of its trajectory was at most 10 s during the experimental runs, the dissolution did not significantly affect the bubble size (constant to within 2%). Thus, the estimated variation in $\beta$ and $\mathscr{L}^*$ (defined in § 2) is less than 3% and 6%, respectively.

The viscous relaxation time of the bubbles was calculated from the relations (see van Wijngaarden & Kapteyn 1990)

$$\tau_b = \frac{a_{eq}^2 Q(\chi)}{18 \nu_l G(\chi)} \tag{11}$$

$$= \frac{V_T}{2g} Q(\chi) \left( 1 + \frac{H(\chi)}{Re^{1/2}} + O(Re^{-5/6}) \right), \tag{12}$$

based on the well-known theory of Moore (1965). Here $\chi$ is the ratio of the lengths of the major and the minor axes of a bubble, assumed to have an ellipsoidal shape. $G(\chi)$ and $Q(\chi)$ are known functions and $H(\chi)$ is available in tabulated form. For bubbles with equivalent radius larger than 0.5 mm $\tau_b$ was estimated from (12), using the measured $V_T$ and values of $\chi$ that were estimated from figure 3 of Duineveld (1995). For smaller bubbles the $O(Re^{-5/6})$ term cannot be neglected and so (11) was used. (For example, in the cases mentioned in table 3, $\chi$ has the value 1.17 for the bubble with radius 0.57 mm, and 1.0 for the bubble with radius 0.34 mm.)

### 3.5. *Bubble tracking technique*

The vertical component and one of the horizontal components of the position of an isolated bubble were measured with a specially developed bubble tracking technique. The set-up (figure 7) consists of: (i) sending optics to illuminate a bubble in the test section of the water tunnel, (ii) receiving optics that collect light scattered by the bubble, (iii) a position-sensitive detector which provides electrical signals from which two coordinates of the bubble position can be determined, (iv) analogue equipment to analyse these signals, and (v) a computer to acquire, process and store the data.

A position-sensitive detector (PSD), rather than a high-resolution CCD camera, is used for measurement of bubble position, since a PSD can offer both high time resolution (sample frequency 1800 Hz for the present set-up) and high effective spatial resolution (typically 1:600). A further advantage of a PSD is that the position of a single bubble is directly proportional to the electrical signals. Determining the position therefore does not require time-consuming image analysis or excessive storage requirements (as would be needed for a CCD camera), which enables collection and processing of large ensembles. A similar method was used independently by Voth, Satyanarayan & Bodenschatz (1998) to track the motion of fluid particles in turbulence, and a related method (with a somewhat different type detector) was described by Call & Kennedy (1991).

The effective spatial resolution with which the bubble position could be measured was limited by the signal-to-noise ratio of the electrical signals. To enhance the signal-to-noise ratio, the signals were measured using coherent detection (e.g. Wilmshurst 1990) with three analogue single-phase Lock-In Amplifiers (Scitech 410). To enable coherent detection the signal was modulated by mechanically chopping the lightbeam in the sending optics at 3000 Hz. The effective bandwith was set to 300 Hz. For a bubble of 0.5 mm radius the effective resolution was typically 0.10 mm in a measurement volume of approximately $60 \times 60 \times 60\ \mathrm{mm}^3$. The analogue signals were processed

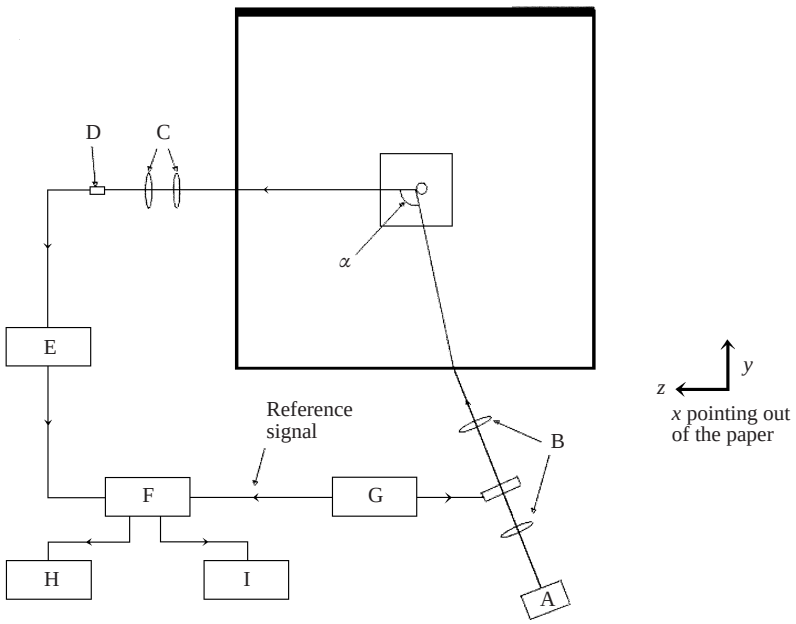


FIGURE 7. Experimental set-up for tracking the bubble position. A, Xenon lamp; B, sending optics; C, receiving optics; D, position-sensitive detector; E, preamplifier; F, lock-in amplifiers (one for each channel) with additional low-pass filters; G, chopper; H, 12 bit AD-converter and computer; I, spectrum analyser.

using a suitably chosen detection and validation scheme. Signals indicating that more than one bubble at a time was present in the measurement volume were rejected.

The bubble velocity was determined using a modified central difference scheme (Snyder & Lumley 1971)

$$V(t_i) \equiv U + \frac{X(t_i+\Delta t) - X(t_i-\Delta t)}{2\Delta t} - \frac{X(t_i+3\Delta t) - 3X(t_i+\Delta t) - 3X(t_i-\Delta t) + X(t_i-3\Delta t)}{24\Delta t}, \tag{13}$$

in which the Eulerian mean fluid velocity $U$ and the bubble position $X$ are measured in the laboratory frame. For this $O(\Delta t^2)$ scheme the spectral transfer function remains unity (as it should) within 10% for frequencies up to about 66 Hz for the time step chosen in our experiments (for an ordinary central difference scheme this already occurs at a frequency that is a factor of 2.44 lower). Reducing $\Delta t$ further would increase this frequency but also increase the mean-square error in the bubble velocity.

Averaged quantities are calculated from an ensemble of identical bubbles. Since the time $T_i$ that a bubble spends in the measurement volume is a random variable, care must be taken to ensure that ensemble-averaged bubble statistics are unbiased. The averaging operator

$$A[f] \equiv \sum_{i=1}^{N} T_i \overline{f}_i \Big/ \sum_{i=1}^{N} T_i \tag{14}$$

was used as approximation to the ensemble average $E[f]$. Here $\overline{f}_i$ is the time average of quantity $f$ of bubble $i$ which was in the measurement volume during time $T_i$. A straightforward calculation (after Bendat & Piersol 1971, ch. 6) demonstrates that

$A[f]$ is a consistent and unbiased estimator, that tends to the ensemble average $E[f]$ asymptotically.

The ensemble-averaged statistics were obtained from at least 1200 bubbles or 230 s total bubble observation time (see table 3). The ensemble-averaged statistics were checked in several ways. The statistically stationary of each ensemble was checked by dividing the entire ensemble chronologically into 10 sub-ensembles. For each sub-ensemble the mean vertical velocity was constant to within $\pm 1.5\%$, while the root-mean-square velocities were constant to within $\pm 3.5\%$. It was checked whether the bubbles statistics were independent of $T_i$, as should be the case if the statistics are unbiased. The mean velocity was independent of $T_i$ to within the statistical variability. However, the root-mean-square velocities were found to decrease with $T_i$, thus indicating a transit time bias in this particular statistic. This decrease is attributed to the finite size of the measurement volume: bubbles with large root-mean-square velocity will disperse fast, hence will not stay long in the measurement volume (small $T_i$). Typically bubbles with $T_i$ less than 0.1 s had a 10% larger root-mean-square velocity than bubbles with $T_i$ larger than 0.9 s, so that this transit time bias is not too serious.

## 4. Experimental results

### 4.1. *Experimental conditions*

The motion of the bubbles was studied in six different turbulent velocity fields constructed by varying the parameters of the forcing protocol of the active grid and by varying the location of the measurement volume with repect to the grid. These velocity fields were verified to have nearly isotropic first-order and second-order statistics. Table 2 lists the relevant flow parameters. The spectrum of case C is shown in figure 2; the shape of the spectrum is similar for the other cases. Cases A, B and C have about equal $L_{11}$ but different $u_0$. Cases A and C (as D and E) have about the same $\mathscr{L}$ and $\lambda$, but different $u_0$. Cases B and F have nearly equal $L_{11}$, $u_0$ and $\lambda$ but different $\mathscr{L}$. Case F has the highest $u_0$ and the smallest $\mathscr{L}$ and thus is expected to induce the strongest inertia effects. Case E has the smallest $u_0$ and is expected to induce the largest effects of drift. The mean velocity was chosen at about $0.3\,\mathrm{m\,s^{-1}}$ so that the bubbles would be convected slowly downwards past the measurement volume.

The parameters associated with bubbles are listed in table 3. Each result represents the average over at least 1200 bubbles or 230 s total observation time. Most of the experiments shown (cases A1–F1) were carried out for bubbles with 0.57 mm radius, about the same size as was used by SB in their numerical experiments. A few experiments (cases B2 and F2) were conducted with smaller bubbles, radius 0.34 mm, to obtain higher values of the non-dimensional turbulence intensity $\beta$. Note that the bubble radius was in all cases larger than the Kolmogorov lengthscale, yet smaller than the Taylor microscale. The volume fraction of gas in the test section was always less than 0.01%, sufficiently small to assume that the turbulence structure is not modified by the presence of the gas bubbles.

### 4.2. *Mean bubble velocity*

Our experimental results concerning the mean rise velocity of spherical gas bubbles in grid-generated turbulence are presented in figure 8; the labels correspond to those in table 3. Error bars indicate the experimental uncertainty, which is about 6% of $V_T$. For comparison the theoretical and numerical results of SB have been included; the

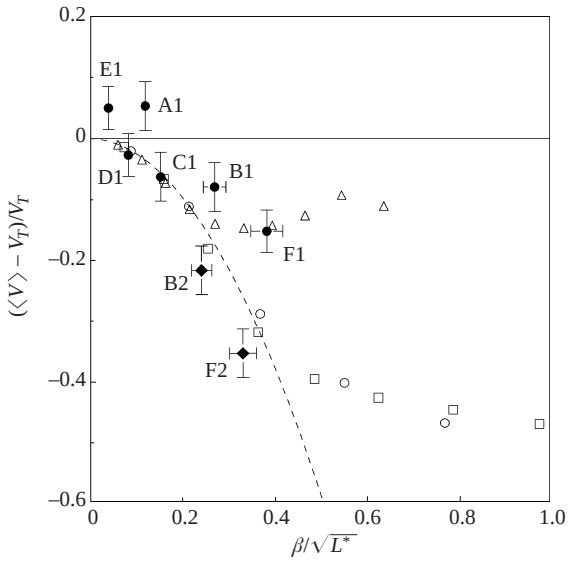


FIGURE 8. Deviation of the mean velocity of rise of a bubble in grid-generated turbulence from its value in still fluid, $\overline{V} - V_T$, made dimensionless with $V_T$. The dashed curve is the analytical result for weak turbulence of intermediate scales of Spelt & Biesheuvel (1997). The open symbols are their data obtained with numerically simulated turbulence with a Kraichnan energy spectrum (square: $\lambda^* = 1$, $\mu = (\pi/2)^{1/2}$) or a von Kármán–Pao energy spectrum (triangle: $\lambda^* = 1$; circle, $\mu = (\pi/2)^{1/2}$). Solid circles are experimental data for bubbles with radius 0.57 mm, solid diamonds for bubbles with radius 0.34 mm. Labels (A1–F1, B2, F2) refer to cases in table 3. Typical errorbars are indicated.

dashed curve is the analytical result for weak turbulence (6), a result that is expected to hold if condition (3) is satisfied. The numerical data of SB (open symbols) are for spherical bubbles of 0.5 mm radius ($V_T = 0.2725\,\mathrm{m\,s^{-1}}$, $\tau_b = 13.9$ ms). Rather than $\beta$, as in figure 3 of SB, we took $\beta/\sqrt{\mathscr{L}^*}$ as the abscissa. This scaling, suggested by (6), should make it easier to compare results obtained for different spectra. Note that for spherical bubbles $\beta/\sqrt{\mathscr{L}^*} = u_0/\sqrt{2g/\mathscr{L}}$ is independent of the bubble parameters.

First, the experiments show that turbulence of the surrounding liquid, even if this is isotropic, can lead to a remarkable reduction in the speed of rise of gas bubbles; a reduction that can be as high as 35% depending on the statistics of the turbulence and the size of the bubbles.

In more detail, it is found that except for case F1, the measured mean rise velocities differ from the theoretical predictions by less than 9% of $V_T$, even though only in cases A1, C1, D1 and E1 is condition (3) strictly satisfied. For cases B1 and F1, which give higher mean rise velocities than predicted by the theory, $\mathscr{L}^*$ is not large compared to $\beta$ (cf. tables 2 and 3) so that a good agreement between theory and experiment would be fortuitous. In cases A1 and E1 the experiments show an increase in mean rise velocity, which clearly disagrees with the theoretical prediction, and for which we have no explanation.

Despite this, an overall difference between theory and experiment of less than 9% is good, and we believe that this is indirect evidence for the validity of the equation of motion of the bubbles (1). In the derivation of this equation it is assumed that the liquid velocity and its gradients can be approximated by linear functions on the scale of the bubble; so formally the ratio of the bubble radius to the Kolmogorov lengthscale $a_e/\eta_K$ should be small compared to unity, for the equation to be applicable.

This condition is not satisfied in all the experiments ($a_e/\eta_K$ is about 3 for the cases C1, B2 and F2) yet the agreement with a theoretical consequence of the use of this equation of motion is good. This suggests, as was assumed by SB, that the restriction on the ratio $a_e/\eta_K$ can be relaxed.

The presentation of the numerical data of SB in the scaling shown in figure 8 also leads to an interesting new result. The numerical results for a Kraichnan spectrum function and a von Kármán–Pao spectrum function with equal non-dimensional integral lengthscale $\mu = L_{11}/(\tau_b V_T)$, collapse on a single curve for all values of $\beta/\sqrt{\mathscr{L}^*}$; note that these spectra have different non-dimensional Taylor microscale $\lambda^*$ and intermediate scale $\mathscr{L}^*$. On the other hand, the numerical data for a von Kármán–Pao spectrum with a constant $\lambda^*$ equal to that of the Kraichnan spectrum is seen to behave quite differently. Thus it appears that the mean rise velocity of the bubbles depends on just two dimensionless numbers: $\beta/\sqrt{\mathscr{L}^*}$ and $\mu$. Data obtained for turbulence energy spectra with equal dimensionless integral scale $\mu$ collapse on a single curve when plotted against $\beta/\sqrt{\mathscr{L}^*}$, and all these curves parameterized by $\mu$ converge to the single curve (6) found by SB, as $\beta/\sqrt{\mathscr{L}^*}$ becomes small. In other words,

$$\frac{\overline{V} - V_T}{V_T} = -\tfrac{3}{4}\pi\beta^2 \frac{1}{\mathscr{L}^*} F(\beta/\sqrt{\mathscr{L}^*}, \mu),$$

where $F$ is a dimensionless function with the property that $F = 1$ in the limit $\beta/\sqrt{\mathscr{L}^*} \to 0$, at arbitrary $\mu$. At finite (but fixed) $\beta/\sqrt{\mathscr{L}^*}$, $F$ decreases if $\mu$ increases.

### 4.3. *Bubble velocity fluctuations*

The measured probability density function of the bubble velocity in the direction of gravity, pdf($V_x$), is shown for case F1 in figure 9($b$) and for case B2 in figure 10($b$). For comparison numerical results obtained from Kinematic Simulation by Spelt (1996) are shown in figures 9($a$) and 10($a$). In each of the cases the median of the p.d.f. occurs at a velocity less than $V_T$, indicating that the bubbles are slowed down on average. For comparison, Gaussian distributions are included. These are defined by the mean and variance of the bubble velocity. The variance was corrected for uncorrelated noise.

The numerically calculated p.d.f. in Figure 9($a$) is significantly asymmetric: the probability that the vertical bubble velocity is about $V_T$ or much less than the average (less than $0.1\,\mathrm{m\,s^{-1}}$, say) are both larger than would be expected for a Gaussian distribution with the same mean and variance (dashed line). Qualitatively, the same behaviour is observed in the experiment (figure 9$b$). Quantitatively, the behaviour is different (though the values of $\beta$ and $\mathscr{L}^*$ are comparable for simulation and experiment, the values of $\mu$ and $\lambda^*$ are quite different). The asymmetric shape of the p.d.f. can be explained as follows. The flow fields in both simulation and experiment correspond to weak turbulence with intermediate scales (i.e. $\beta \approx 0.2$, $\mathscr{L}^* \approx 0.4$). In this regime the lift force drives the bubble preferentially into 'downflow regions' (see SB). Suppose that fraction $\gamma$ of the turbulence consists of 'downflow regions' (the precise definition of these structures is irrelevant here) while fraction $1-\gamma$ consists of other structures. The preferential attraction of bubbles to downflow regions implies that the fraction of time a bubble spends in these regions is larger than $\gamma$. Hence the contribution of downflow regions to the statistics of the bubble velocity will also be larger than $\gamma$, which means that the probability of a bubble velocity much lower than $V_T$ is higher than that for a Gaussian distribution. Since the area under the p.d.f. must remain unity, the probability must be lower than that of a Gaussian p.d.f. for other velocities.

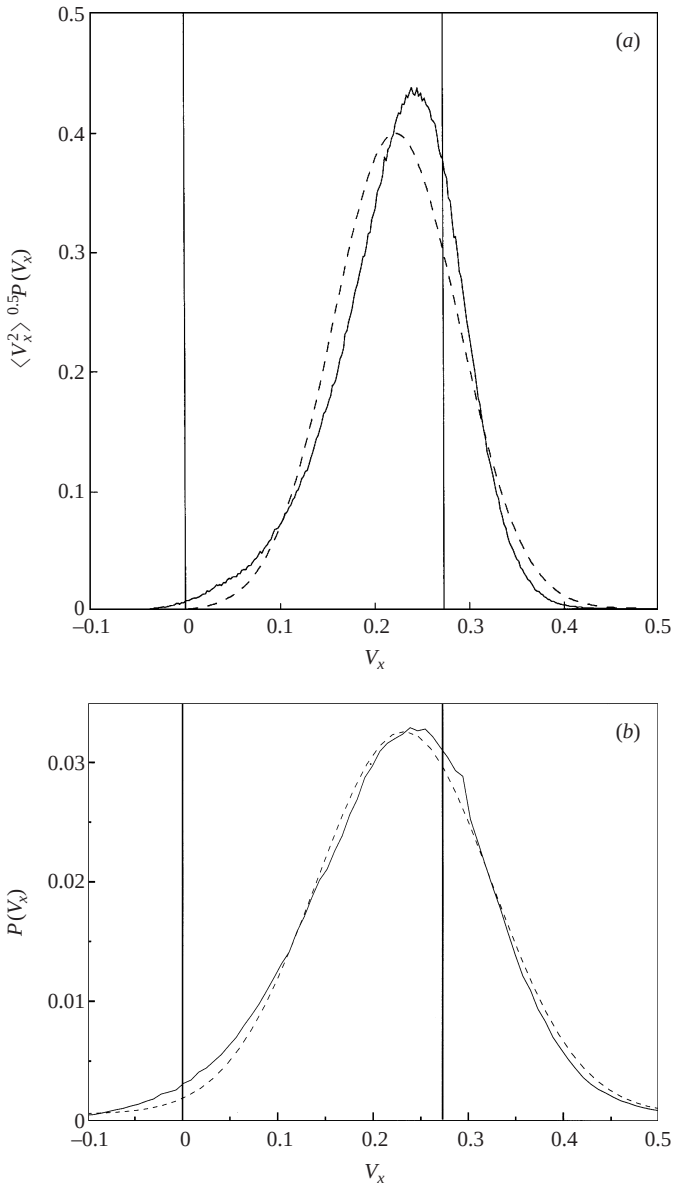


FIGURE 9. Probability distribution function of the vertical bubble velocity. Dashed lines are Gaussian fits. Vertical lines indicate $V_x = 0$ and $V_T$, the rise velocity in still fluid. (*a*) Kinematic Simulation by Spelt & Biesheuvel (1997) with a Kraichnan spectrum function ($\beta = 0.18$, $\mu = 1.25$, $\mathscr{L}^* = 0.47$, $\lambda^* = 1.0$). (*b*) Experiment for case F1 ($\beta = 0.21$, $\mu = 5.70$, $\mathscr{L}^* = 0.30$, $\lambda^* = 0.54$).

For larger $\beta$ and $\mathscr{L}^*$ the numerically calculated p.d.f. (figure 10*a*) is asymmetric in the opposite direction, and qualitatively the same is found experimentally for case B2 (figure 10*b*). As before, this asymmetry indicates that the statistics of the turbulence sampled by the bubble is biased. However, the different shape of the asymmetry indicates that the mechanism for this bias is different than in the case described above. This point was also investigated by SB. They found differences in the statistics sampled by the bubble, depending on the values of $\beta$ and $\lambda^*$. As $\beta$ increases: (i) the

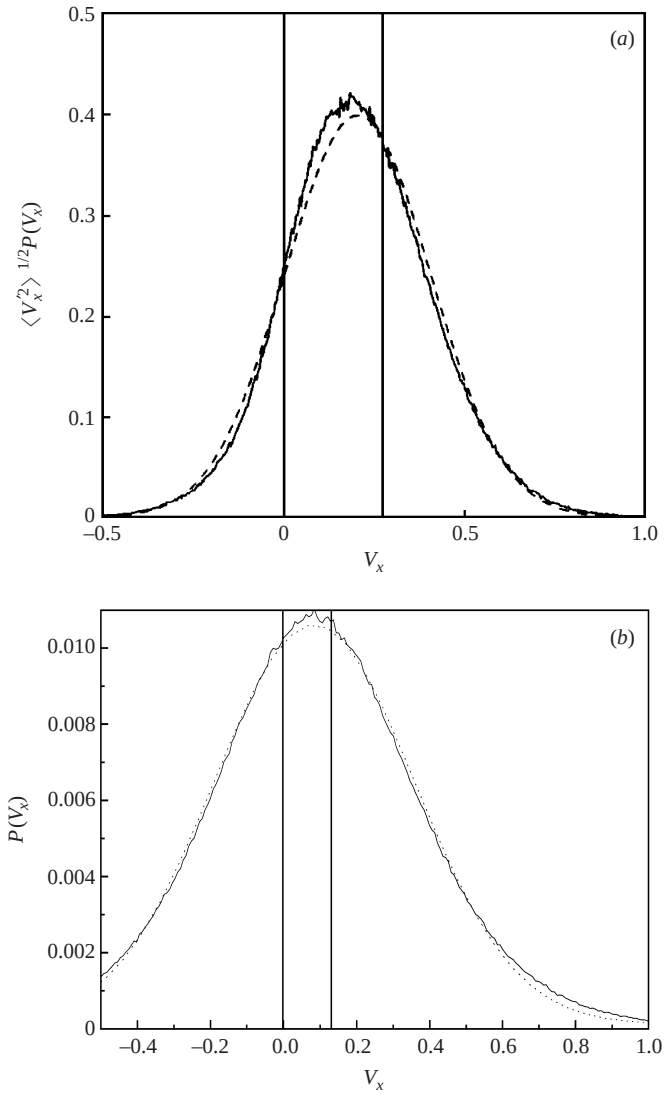


FIGURE 10. As figure 9 but for (*a*) $V_T = 0.27\,\mathrm{m\,s^{-1}}$, $\beta = 0.66$, $\mu = 5.01$, $\mathscr{L}^* = 1.88$, $\lambda^* = 4.0$, and (*b*) case B2 ($V_T = 0.13\,\mathrm{m\,s^{-1}}$, $\beta = 0.44$, $\mu = 43.0$, $\mathscr{L}^* = 2.44$, $\lambda^* = 3.56$).

probability that a bubble is in an 'eddy zone' increases (their figure 6), and (ii) the structures in which bubbles tend to accumulate change from 'downflow regions of large extent' into 'downwards flowing edges of vortices' (their figure 7). A deeper study into the interaction between bubbles and vortical structures in flow fields is needed to give further insight.

Not shown here is that the p.d.f. of the velocity fluctuations in the lateral direction was found to be close to Gaussian in all cases studied; it must be symmetric of course, since the turbulence is homogeneous.

### 4.4. *Dispersion of the bubbles*

The displacement of a bubble is defined by $X(\tau) \equiv X_m(t+\tau) - X_m(t)$, in which $X_m$ denotes the measured bubble position in the laboratory frame. The p.d.f. of the bubble

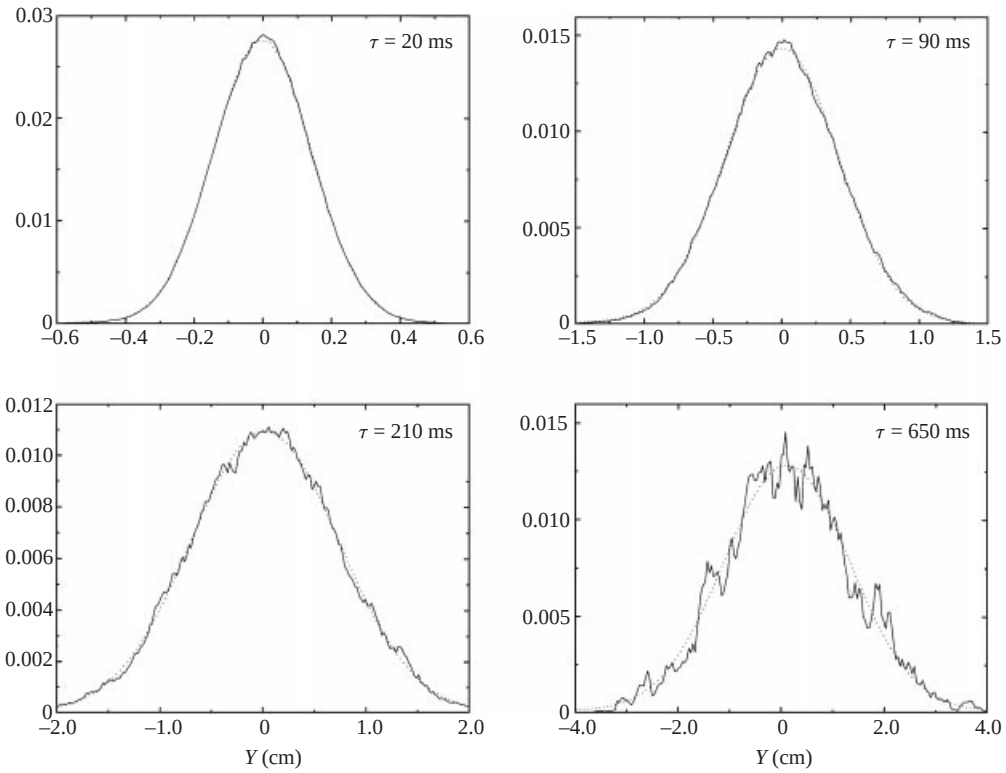


FIGURE 11. Probability distribution function of the horizontal displacement of a bubble in a fixed time lag for case C1. The time lags $\tau = 20$, 90, 210 and 650 ms are approximately equal to $\lambda/V_T$, $\lambda/u_0$, $L_{11}/V_T$ and $L_{11}/(2u_0)$, respectively. Dotted lines indicate a Gaussian distribution.

displacement in the horizontal direction for case C1 is shown for four fixed values of $\tau$ in figure 11. The measured distributions are close to Gaussian. For increasing $\tau$, fewer samples are available in the ensemble, hence the statistical variability increases with $\tau$. The same Gaussian behaviour was found for all other cases of table 3. This Gaussian behaviour is consistent with the numerical results of SB at somewhat different values of the parameters (Kraichnan spectrum, $\beta = 0.53$ and $\mu = 2$).

The p.d.f. of the bubble displacement in the vertical direction for case C1 is shown for two fixed values of $\tau$ in figure 12. Note that the maximum of the distribution shifts to smaller $X$ with increasing $\tau$ because the bubbles are convected in the negative $X$-direction on average. The measured distribution of the vertical displacement is also close to Gaussian. Nevertheless, unlike that of the horizontal displacement, it is slightly skewed. This phenomenon can be understood from the skewness of the vertical bubble velocity distribution shown in the previous section. The displacement of a bubble is a time integral of the bubble velocity and therefore, if the velocity distribution is skewed, one would expect that the displacement distribution is skewed in the same way.

A Gaussian displacement for all times implies that the dispersion can be described by a diffusion process (e.g. Batchelor 1949), with an associated diffusion coefficient that is a function of time. Now, a measure for the dispersion of bubbles by turbulence is the mean-square displacement

$$D \equiv \overline{(X(\tau) - \overline{X(\tau)})^2},$$

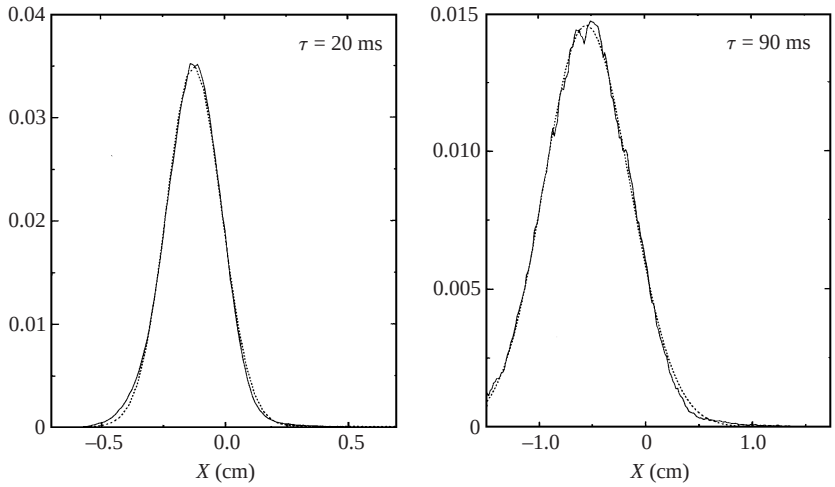


FIGURE 12. Probability distribution function of the vertical displacement of a bubble in a fixed time lag for case C1. The time lags $\tau = 20$ ms and 90 ms are approximately equal to $\lambda/V_T$ and $\lambda/u_0$, respectively. Dotted lines indicate a Gaussian distribution.

which is related to the measured position by

$$D = \overline{(X_m(t+\tau) - X_m(t) - (\overline{X_m(t+\tau) - X_m(t)}))^2}$$
$$= \overline{(X_m(t+\tau) - X_m(t))^2} - \tau^2(\overline{V_m})^2,$$

since $\overline{X_m(t+\tau) - X_m(t)} = \overline{V_m}\tau$. Note that this equality is valid for an arbitrary inertial frame. Half the rate of change of $D$ is called the diffusion coefficient

$$\mathscr{D}_\alpha(\tau) \equiv \frac{1}{2}\frac{\partial}{\partial\tau}\overline{(X_\alpha(\tau) - \overline{X_\alpha(\tau)})^2}, \tag{15}$$

where $\alpha$ denotes the coordinate (no summation over Greek indices). The limiting values of $\mathscr{D}_\alpha$ for small and large times are

$$\mathscr{D}_\alpha(\tau) = \begin{cases} \overline{v_\alpha^2}\tau & (\tau \to 0), \\ \overline{v_\alpha^2}\mathscr{T}_\alpha & (\tau \to \infty). \end{cases} \tag{16}$$

Here $\overline{v_\alpha^2}$ and $\mathscr{T}_\alpha$ are the mean-square bubble velocity and integral timescale, respectively. If (i) the bubble velocity is statistically stationary and (ii) $\mathscr{T}_\alpha$ is finite, the limit for $\tau \to \infty$ of $\mathscr{D}_\alpha(\tau)$ exists and the limiting value, $\mathscr{D}_\alpha(\infty)$, is usually referred to as the diffusivity. It is this diffusivity for which relations were given in § 2. To avoid the errors due to differentiation with respect to $\tau$ a 'pseudo-diffusion coefficient' $\mathscr{D}'$ is computed as

$$\mathscr{D}'_\alpha(\tau) = \frac{1}{2\tau}\overline{\left(X_\alpha(\tau) - \overline{X_\alpha(\tau)}\right)^2}.$$

If $\mathscr{D}$ tends to a constant value for large $\tau$ (as it should), then the values of $\mathscr{D}'$ and $\mathscr{D}$ will be equal at large $\tau$. This allows one to infer the diffusivity $\mathscr{D}$ from the asymptotic value of $\mathscr{D}'$.

It was found in all cases that $\mathscr{D}/u_0L_{11} < 0.08$, which is considerably lower than the diffusivity of fluid particles, $\mathscr{D}_{fp}/u_0L_{11} = 0.53$ (e.g. SB). This reduction is attributed to the crossing trajectories effect (Csanady 1963), which becomes increasingly more

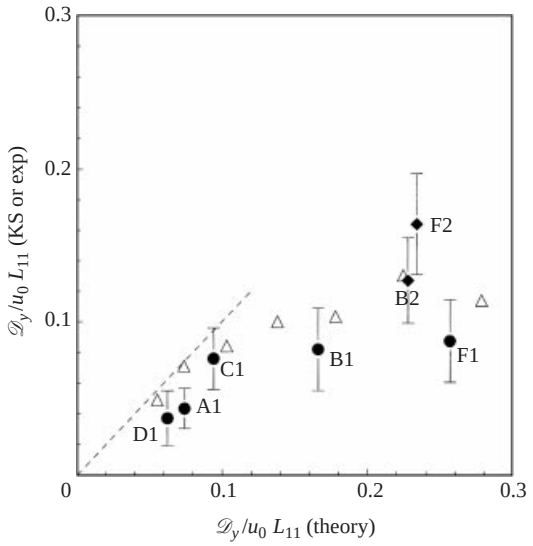


FIGURE 13. Measured and simulated horizontal diffusivity, $\mathscr{D}_y(\infty)/u_0 L_{11}$, plotted versus the theoretical diffusivity. Open triangles, numerical simulations, von Kármán–Pao spectrum with $\lambda^* = 1$ (Spelt & Biesheuvel 1997). Solid circles, experiments for cases A1, B1, C1, D1 and F1. Solid diamonds, experiments for cases B2 and F2. Typical errorbars are indicated.

important with decreasing values of $\beta$. In figure 13 the measured lateral diffusivity, i.e. the value for large $\tau$ of the diffusion coefficient defined by (15), is compared with the theoretical result (9) derived by SB. That relation includes three non-dimensional parameters (i.e. $\beta$, $\mu$ and $\mathscr{L}^*$) which are varied simultaneously in the experiments. To allow a comparison the experimental results are plotted versus the theoretical result, which, it should be noted, is derived under the assumption that $\beta$ is very small compared to unity. Also included are data from numerical simulations of SB for a spectrum with values of $\mathscr{L}^*$ and $\mu$ that are comparable to those in the experiments. It is found that the first two points of the numerical simulations (which correspond to the lowest values of $\beta$, i.e. $\beta = 0.053$ and 0.111, respectively) coincide with the theoretical result. For larger values of $\beta$ the numerically and experimentally determined diffusivities are consistent with each other, but lower than the analytical result.

The above agreements between simulations and experiments for statistics that depend on details of flow structures in the turbulence (e.g. the pdf($V_x$) shown above) are evidence that the Kinematic Simulation qualitatively captures the flow structures relevant for the dispersion of the bubbles. Recently, Malik & Vassilicos (1999) reached a similar conclusion concerning the relative dispersion of fluid particles; they found good qualitative and satisfactory quantitative agreement between their data obtained with Kinematic Simulation, and the DNS data of Yeung (1994).

## 5. Conclusions

The motion of spherical and nearly spherical bubbles in nearly isotropic turbulence behind an active grid was investigated experimentally. The design of this active grid followed that of the grids developed by Makita (1991) and Mydlarski & Warhaft (1996) for use in wind tunnels. It was found that by minor changes in the geometry of the agigator wings and in the forcing protocol that governs their random flapping the

isotropy of the turbulence could be remarkably improved. With our grid, microscale Reynolds numbers up to 200 could be achieved.

The motion of the bubbles was tracked with a novel optical technique that uses a position-sensitive detector. This accurate technique, a modification of that developed by Call & Kennedy (1991), allows the position in two dimensions of a single bubble to be tracked. Compared with the traditional CCD camera the spatial resolution is good, the time resolution is even better, and storage and processing times are orders of magnitude less due to the analogue nature of the technique.

The experimental results on the bubble motion were compared with theoretical results and results from numerical simulations presented by Spelt & Biesheuvel (1997). The reduction in average rise velocity of the bubbles depends on the structure of the turbulence and can be as high as 35%. For weak turbulence with moderate characteristic lengthscales, the experimentally determined reduction in average rise velocities agreed within 9% with the theoretically determined value. This good agreement suggests that the equation of motion used in the analysis applies well for the cases considered, even though the bubble radius is not small compared to the Kolmogorov lengthscale of the turbulence and in some of the experiments the bubbles were slightly oblate (ratio of the major axis to the minor axis approximately 1.17).

Regarding the other statistics of the bubble motion, it was found that the p.d.f.s of the lateral displacement and velocity are close to Gaussian for all cases considered. On the other hand, the p.d.f.s of the longitudinal displacement and velocity are asymmetric and hence non-Gaussian. The degree of departure from Gaussianity depends on the values of the non-dimensional parameters that characterize intensity and lengthscales of the turbulence in comparison to the bubble rise velocity and relaxation time (i.e. $\beta$, $\mathscr{L}^*$ and $\mu$). This implies that the dispersion of the gas bubbles in the lateral direction can be regarded as a diffusion process with a diffusion coefficient that is a function of time. Formally this is not true for the dispersion process in the longitudinal direction; but the departure from Gaussianity is small, so that a description as a diffusion process may lead to useful results.

On all points where the experimental data could be compared with data for turbulence generated by Kinematic Simulation (Spelt & Biesheuvel 1997) a good qualitative (and in many cases, quantitative) agreement was found. This suggests that Kinematic Simulation is of value for the prediction of the statistics of the motion of spherical bubbles rising at high Reynolds number in turbulence of moderate intensity (i.e. $\beta$ small enough).

We shall now consider the impact of the above findings on bubbly flows in general. The rise velocity of a bubble in still water $V_T$ and its viscous relaxation time $\tau_b$ are both proportional to the square of the bubble radius $a_e$. This implies that, in a turbulent flow with given intensity, $u_0$ and lengthscales $\mathscr{L}$ and $L_{11}$ and the non-dimensional parameters that characterize the bubble motion (i.e. $\beta = u_0/V_T$, $\mathscr{L}^* = \mathscr{L}/(\tau_b V_T)$ and $\mu = L_{11}/(\tau_b V_T)$) vary rapidly with bubble size. Since the statistics of the bubble motion strongly depend on the values of these non-dimensional parameters, minor differences in the size of the bubbles may result in substantial differences in the reduction of their mean rise velocities or in the root-mean-square values of their velocity fluctuations in grid-generated turbulence. This implies that bubbles of different sizes may contribute in very different ways to the dynamics of turbulent bubbly flows. A theory that assumes that the modification of the turbulence of the liquid phase depends on the local void fraction alone, ignoring effects of the bubble size distribution, may be of limited practical value.

The fact that the statistics of the bubble motion in grid-generated turbulence

depends sensitively on the values of the non-dimensional parameters mentioned above suggests part of the explanation of why upscaling of turbulent bubbly flows, a common practice in the process industry, often has limited success. Discrepancies between experiments at model scale and at full scale may well be related to significantly different values of dimensionless parameters.

We sincerely appreciate all the help received from our colleagues Gert-Wim Bruggert, Wim Gorissen, Henni Scholten, Peter Spelt and Leen van Wijngaarden, and from the students Arjan van Galen, Bas Janssen, Herwin Kleinjan, Marjanca Koetsier, Bart Paarhuis, Frank Schipper and Marc Wolswinkel.

We gratefully acknowledge Maarten Dirkzwager, Hans van Maanen, Dick Passchier, Jaap den Toonder and Mark Tummers of the Dutch Association for Laser Anemometry for valuable advice on LDA and digital processing of stochastic data, and for making available their software for processing LDA data. We also thank Alex Florians, Bart de Grooth and Inge Peters of the Department of Applied Physics for their skillful assistence with the development of the bubble tracking technique.

This work is part of the research program of the "Stichting voor Fundamenteel Onderzoek der Materie (FOM)", which is financially supported by the "Nederlandse organisatie voor wetenschappelijk onderzoek (NWO)".

## REFERENCES

Auton, T. R., Hunt, J. C. R. & Prud'homme, M. 1988 The force exerted on a body in inviscid unsteady non-uniform rotational flow. *J. Fluid Mech.* **197**, 241–257.

Batchelor, G. K. 1949 Diffusion in a field of homogeneous turbulence. I. Eulerian analysis. *Austral. J. Sci. Res.* A **2**, 437–450.

Batchelor, G. K. 1953 *The Theory of Homogeneous Turbulence*. Cambridge University Press.

Bel Fdhila, R. & Duineveld, P. C. 1996 The effect of surfactant on the rise of a spherical bubble at high Reynolds and Peclet numbers. *Phys. Fluids* **8**, 310–321.

Bendat, J. R. & Piersol, A. G. 1971 *Random Data: Analysis and Measurement Procedures.* Wiley.

Call, C. J. & Kennedy, I. M. 1991 A technique for measuring Lagrangian and Eulerian particle statistics in a turbulent flow. *Exps. Fluids* **12**, 125–130.

Csanady, G. T. 1963 Turbulent diffusion of heavy particles in the atmosphere. *J. Atmos. Sci.* **20**, 201–208.

Duineveld, P. C. 1994 Bouncing and coalescence of two bubbles in water. PhD thesis, University of Twente.

Duineveld, P. C. 1995 The rise velocity and shape of bubbles in pure water at high Reynolds number. *J. Fluid Mech.* **292**, 325–332.

Eppinger, K. 1995 Etude du mouvement des bulles dans une turbulence homogène isotrope. PhD thesis, Institut de Mécanique des Fluides de Toulouse.

Fung, J. C. H., Hunt, J. C. R., Malik, N. A. & Perkins, R. J. 1992 Kinematic simulation of homogeneous turbulence by unsteady random Fourier modes. *J. Fluid Mech.* **230**, 281–318.

Legendre, D. & Magnaudet, J. 1998 The lift force on a spherical bubble in a viscous linear shear flow. *J. Fluid Mech.* **368**, 81–126.

Ling, S. C. & Wan, C. A. 1972 Decay of isotropic turbulence generated by a mechanically agitated grid. *Phys. Fluids* **15**, 1363–1369.

van Maanen, H. R. E. & Oldenziel, A. 1998 Estimation of turbulence power spectra from randomly sampled data by curve-fit to the autocorrelation function applied to laser Doppler anemometry. *Meas. Sci. Technol.* **9**, 458–467.

Makita, H. 1991 Realization of a large-scale turbulence field in a small wind tunnel. *Fluid Dyn. Res.* **8**, 53–64.

Makita, H. & Sassa, K. 1991 Active turbulence generation in a laboratory wind tunnel. In *Advances in Turbulence 3* (ed. A. V. Johansson & P. H. Alfredsson), pp. 497–505. Springer.

Malik, N. A. & Vassilicos, J. C. 1999 A Lagrangian model for turbulent dispersion with turbulent-like flow structure: comparison with DNS for two-particle statistics. *Phys. Fluids* **11**, 1572–1580.

Maxey, M. R. 1987 The gravitational settling of aerosol particles in homogeneous turbulence and random fields. *J. Fluid Mech.* **174**, 441–465.

Maxey, M. R., Chang, E. J. & Wang, L.-P. 1994 Simulation of interactions between microbubbles and turbulent flows. *Appl. Mech. Rev.* **47**, S70–S74.

Mei, R. 1994 Effect of turbulence on the particle settling velocity in the nonlinear drag range. *Intl J. Multiphase Flow* **20**, 273–284.

Mei, R., Adrian, R. J. & Hanratty, T. J. 1991 Particle dispersion in isotropic turbulence under Stokes drag and Basset force with gravitational settling. *J. Fluid Mech.* **225**, 481–495.

Mei, R., Adrian, R. J. & Hanratty, T. J. 1997 Turbulent dispersion of heavy particles with nonlinear drag. *Trans. ASME: J. Fluids Engng* **119**, 170–179.

Mohamed, M. S. & LaRue, J. C. 1990 The decay power law in grid-generated turbulence. *J. Fluid Mech.* **217**, 195–214.

Moore, D. W. 1965 The velocity of rise of distorted gas bubbles in a liquid of small viscosity. *J. Fluid Mech.* **23**, 749–766.

Mydlarski, L. & Warhaft, Z. 1996 On the onset of high-Reynolds-number grid-generated wind tunnel turbulence. *J. Fluid Mech.* **320**, 331–368.

Nir, A. & Pismen, L. M. 1979 The effect of a steady drift on the dispersion of a particle in turbulent fluid. *J. Fluid Mech.* **94**, 369–381.

Ooi, K. K. & Acosta, A. J. 1984 The utilization of specially tailored air bubbles as static pressure sensors in a jet. *Trans. ASME: J. Fluids Engng* **106**, 459–465.

Poorte, R. E. G. 1998 On the motion of bubbles in active grid generated turbulent flows. PhD thesis, University of Twente.

Sene, K. J., Hunt, J. C. R. & Thomas, N. H. 1994 The role of coherent structures in bubble transport by turbulent shear flows. *J. Fluid Mech.* **259**, 219–240.

Snyder, W. H. & Lumley, J. L. 1971 Some measurements of particle velocity autocorrelation functions in a turbulent flow. *J. Fluid Mech.* **48**, 41–71.

Spelt, P. D. M. 1996 On the motion of bubbles in a turbulent flow. PhD thesis, University of Twente.

Spelt, P. D. M. & Biesheuvel, A. 1997 On the motion of gas bubbles in homogeneous isotropic turbulence. *J. Fluid Mech.* **336**, 221–244 (referred to herein as SB).

Spelt, P. D. M. & Biesheuvel, A. 1998 Dispersion of gas bubbles in large-scale homogeneous isotropic turbulence. *Appl. Sci. Res.* **58**, 464–482.

Tummers, M. J. & Passchier, D. M. 1996 Spectral estimation using a variable window and the slotting technique with local normalization. *Meas. Sci. Technol.* **7**, 1541–1546.

Voth, G. A., Satyanarayan, K. & Bodenschatz, E. 1998 Lagrangian acceleration measurements at large Reynolds numbers. *Phys. Fluids* **10**, 2268–2280.

Wang, L.-P. & Maxey, M. R. 1993*a* The motion of microbubbles in a forced isotropic and homogeneous turbulence. *Appl. Sci. Res.* **51**, 291–296.

Wang, L.-P. & Maxey, M. R. 1993*b* Settling velocity and concentration distribution of heavy particles in homogeneous isotropic turbulence. *J. Fluid Mech.* **256**, 27–68.

van Wijngaarden, L. & Kapteyn, C. 1990 Concentration waves in dilute bubble/liquid mixtures. *J. Fluid Mech.* **212**, 111–137.

Wilmshurst, Y. H. 1990 *Signal Recovery from Noise in Electronic Instrumention.* IOP Publishing Ltd.

Yeung, P. K. 1994 Direct numerical simulation of two-particle relative diffusion in isotropic turbulence. *Phys. Fluids* **6**, 3416–3428.